A two-way nested global-regional dynamical core on the cubed-sphere grid

LUCAS M. HARRIS

Program in Atmospheric and Oceanic Sciences, Princeton University, Princeton, NJ *

SHIAN-JIANN LIN

NOAA/Geophysical Fluid Dynamics Laboratory, Princeton University, Princeton, NJ

* *Corresponding author address:* Lucas Harris, Geophysical Fluid Dynamics Laboratory, Princeton University, Forrestal Campus, 201 Forrestal Road, Princeton, NJ, 08540-6649

E-mail: Lucas.Harris@noaa.gov

ABSTRACT

A nested-grid model is constructed using the Finite-Volume dynamical core on the cubed sphere. The use of a global grid avoids the need for externally-imposed lateral boundary conditions, and a consistent solution is produced by using the same governing equations and discretization on the global and regional domains. A simple interpolated nested-grid boundary condition is used, and two-way updates use a finite-volume averaging method that conserves scalar quantities and vorticity. In particular, mass conservation in a two-way nested simulation is achieved by simply not updating the mass field, which eliminates the need for carefully-constructed flux boundary conditions. Despite the simplicity of the nesting methodology, nested-grid simulations of a series of common idealized test cases show favorable results, as the large-scale solutions are not corrupted by the nested grid. We also show evidence that the nested grid is able to improve the coarse-grid solution, even beyond the boundaries of the nest.

1. Introduction

Global models have many advantages for climate simulation and medium-range weather prediction. Global models do not need externally-imposed lateral boundary conditions (BCs), and so there are no issues with boundary errors contaminating the solution, nor inconsistency between the model dynamics and that of the imposed BCs, two major problems for limited-area models (Warner et al. 1997). Global models also allow synoptic- and planetary-scale features to be better represented and to interact with any smaller-scale features that may be resolved by the model. This scale interaction is particularly important for studies of orographic drag and deep convection on the general circulation, and in forecasting hurricanes and other phenomena that feed back onto their large-scale environment.

However, running a global model with uniform grid spacing at scales needed to fully resolve these features is still impractical using today's computers. Regional climate models (RCMs; Giorgi and Mearns 1999) typically require years- or decades-long simulations of phenomena that may only be dozens of kilometers wide, and accurate hurricane intensity forecasting may require resolving features only a few kilometers wide. For this reason many RCMs and hurricane models use a limited domain with boundary conditions supplied by a global model with comparatively low resolution and only available at coarse time intervals. The resolution, discretization, and even the governing equations can differ between the global and limited-area model, and these inconsistencies lead to boundary errors. The features resolved by the limited-area model are also unable to feed back onto the global domain, which is perhaps the most significant disadvantage of a limited-area domain for RCMs and medium-range forecasting.

A better solution would be to use a global model with a locally refined grid, which would represent the large scales globally, use the higher resolution only over the area of interest, and allow the two scales to interact. While any grid refinement will cause errors as disturbances propagate through the refined region, we expect that having the refined and coarse regions in the same model (complete with the same dynamics and discretization), and having the large-scale data continually supplied to the refined region, would yield smaller boundary errors than if a regional model were to be forced with boundary data from an independent, non-interacting global model. The simplest and most common approach is to use a stretched or deformed grid, a deformed uniform-resolution grid having more grid points or cells clustered over the region of interest. On the opposite side of the globe (which we are presumably less interested in) there are fewer gridpoints, as depicted in Figure 1. This capability already exists in several models, including that described in this paper; see Courtier and Geleyn (1988) and Fox-Rabinovitz et al. (2006) for other examples. However, if the stretching is enough that the grid size varies significantly, new problems can occur. The timestep of the entire grid will be controlled by the smallest grid spacing in the refined region, which increases the computational expense of the simulation. Further, since physical parameterizations are often scale-dependent, unless special parameterizations that adapt to the grid spacing are used, they may only be appropriate for certain parts of the model domain. Finally, the resolution on the side opposite to the refined region may be so much more coarse than in the rest of the domain that disturbances passing through this region may no longer be well-enough resolved to be represented accurately. The resulting errors can propagate into the refined region if the simulation is long enough.

A much less common approach is to use a two-way nested model (Figure 1), with the global domain acting as the coarse, "parent" grid and a regional domain acting as the nested grid, with nested-grid BCs periodically applied from the global grid. Both grids use the same model dynamics and discretization, so the only inconsistency arises from the different resolutions of the two grids. Applying different timesteps and physical parameterizations between the two grids is trivial, and the coarse grid domain need not be altered to allow nesting; in particular grid nesting does not require a decrease in global model resolution anywhere, and nests can be placed at an arbitrary number of locations on the globe, or even within one another. Two-way nesting allows for the nested grid to influence the global grid by periodically "updating" or replacing the global solution by the nested-grid solution where the grids coincide. Nested grids are also more versatile than stretched grids, as any number of nested grids can be used, grids can be nested within one another, and nests can be rectangular instead of just square. Drawbacks of two-way nesting are that the grid boundary is a discontinuous refinement and creates more localized errors than does a gradual refinement, and that interaction between the refined and coarse regions only occurs at defined intervals (typically more frequently than the externally-imposed BCs for limited-area models), while for a stretched grid this interaction occurs naturally at every timestep.

The authors are aware of a few studies using two-way global-to-regional nested models. Lorenz and Jacob (2005) nested a regional gridpoint model in a spectral global model for a ten-year climate integration, in order to better represent the topography of the maritime continent. Their results were promising—a global decrease in zonally-averaged temperature biases was observed in the nested model compared to the single-grid global model—but no further results were shown and no further research using this model appears to exist. Inatsu and Kimoto (2009) found a result similar to, but less compelling, than that of Lorenz and Jacob (2005), using a similar nesting methodology with a nest over northeast Asia. Chen et al. (2011) used a two-way nested RCM which placed a nest over eastern China, using the same gridpoint model for both the global and nested grids. They found a local reduction in temperature bias, but did not examine the effect of two-way nesting outside of the nested region.

Dudhia and Bresch (2002) presented a test of global-to-regional two-way nesting using the global version of the Pennsylvania State University-National Center for Atmospheric Research Mesoscale Model (MM5) for a three-day weather forecast for North America. The 40-km grid-spacing nested grid was able to resolve features that the 120-km grid-spacing global domain could not, with apparently a minimum of distortion at the nested-grid boundary. Similar capability exists in the Weather Research and Forecasting (WRF) model (Richardson et al. 2007). The TM5 model (Krol et al. 2005) and the GEOS-CHEM model (Bey et al. 2001) are both "offline" chemistry and transport models which can use two-way global-to-regional nesting, but are not dynamical models and rely on reanalysis data or model output from other sources to operate.

In this paper we present a two-way nested idealized model using the Finite-Volume (FV) formulation of Lin (2004, henceforth L04), discretized on the cubed-sphere geometry of Putman and Lin (2007, henceforth PL07). This dynamical core has been very successful in a number of applications, including climate simulation (Delworth et al. 2006; Donner and coauthors 2011), weather prediction (Lin et al. 2004; Atlas et al. 2005), and seasonal hurricane prediction (Zhao et al. 2009; Chen and Lin 2011). Both the nested and coarse grids use the same FV core, ensuring consistency between the grids. Any of a number of schemes for the grid coupling can be used in our nested-grid model, although we will find that favorable results can be attained using simple, standard methods, including a straightforward method for conserving mass on the global coarse grid.

The model will be tested using several common idealized test cases. The first is the baroclinic instability test case of Jablonowski and Williamson (2006) which tests the ability of the nesting to permit individual disturbances to pass into and out of the nested grid region and to yield a reasonable solution on timescales of one to two weeks. The second is the idealized climate integration of Held and Suarez (1994) which tests the ability of the nested model to preserve the climatology produced during a multiple-year integration. A third uses real topography and initial conditions to demonstrate how grid nesting can improve the coarse-grid's representation of vortex shedding in the lee of the Island of Hawaii, even beyond the extent of the nested grid. Two more tests are performed with a shallow-water version of the model to demonstrate how well the FV core and grid geometry maintains solutions of the governing equations.

Section 2 describes the FV core, cubed-sphere grid geometry, and the nesting methodology. Section 3 describes the results from the test cases. Section 4 concludes the paper.

2. The Nested Grid Model

a. Finite-Volume Dynamical Core and cubed-sphere grid

The FV core is a hydrostatic, 3D dynamical core using the vertically-Lagrangian discretization of L04 and the horizontal discretization of Lin and Rood (1996, 1997, henceforth LR96 and LR97, respectively), using the cubed-sphere geometry of PL07 and Putman (2007). This solver divides a hydrostatic atmosphere into a number of vertical layers, each of which is then integrated treating the pressure thickness and potential temperature as scalars. Each layer is advanced independently, except that the pressure gradient force is computed using the geopotential and the pressure at the interface of each layer (Lin 1997). The interface geopotential is the cumulative sum of the thickness of each underlying layer, counted from the surface elevation upwards, and the interface pressure is the cumulative sum of the pressure thickness of each overlying layer, counted from the constant-pressure top of the model domain downward. Vertical transport occurs implicitly from horizontal transport along Lagrangian surfaces. The layers are allowed to deform freely during the horizontal integration. To prevent the layers from becoming infinitesimally thin, and to vertically re-distribute mass, momentum, and energy, the layers are periodically remapped to a pre-defined Eulerian coordinate system.

The governing equations in each horizontal layer are the vector-invariant shallow-water[1] equations:

$$
\begin{aligned}
\frac{\partial \delta p}{\partial t} + \nabla \cdot (\mathbf{V}\delta p) &= 0 \\
\frac{\partial \delta p \Theta}{\partial t} + \nabla \cdot (\mathbf{V}\delta p \Theta) &= 0 \\
\frac{\partial \mathbf{V}}{\partial t} &= -\Omega \hat{k} \times \mathbf{V} - \nabla\left(\kappa + \nu \nabla^2 D\right) - \frac{1}{\rho}\nabla p\Big|_z
\end{aligned}
$$

[1]The individual layers are not true shallow-water layers since the potential temperature, and thus density, is not homogeneous in each layer; however, since the density only explicitly enters through the pressure gradient force in (3) and (4) the equations solved are identical to the shallow-water equations with the (hydrostatic) pressure in place of height.

where the prognostic variables are the pressure thickness δp of a layer bounded by two adjacent Lagrangian surfaces, which in this hydrostatic system is the mass of the layer; the potential temperature Θ; and the vector wind $\mathbf{V}$. Here, $\hat{k}$ is the vertical unit vector. The other variables are diagnosed: the density ρ, kinetic energy $\kappa = \frac{1}{2}\|\mathbf{V}\|$, divergence D, pressure p, and absolute vertical vorticity Ω. Finally, the prescribed higher-order ∇^4 divergence damping strength is given by ν.

The system can be horizontally discretized in orthogonal coordinates, as on the latitude-longitude grid (LR97); however, on the cubed sphere an orthogonal coordinate yields cells which become dramatically smaller near the corners of the cube. We instead adopt the gnomonic coordinate of PL07, in which coordinate lines are great circles. This coordinate yields more uniformly-sized cells over the whole sphere, but is non-orthogonal. As a result, the prognosed covariant wind components u and v differ from the diagnosed contravariant wind components $\widetilde{u}$ and $\widetilde{v}$ which are required for the transport operator. Define $\mathbf{V} = \widetilde{u}\mathbf{e_x} + \widetilde{v}\mathbf{e_y}$, where $\mathbf{e_x}$ and $\mathbf{e_y}$ are the local unit vectors of the coordinate system. The covariant components of the wind are then $u = \mathbf{V} \cdot \mathbf{e_x}$ and $v = \mathbf{V} \cdot \mathbf{e_y}$, and the kinetic energy is $\kappa = \frac{1}{2}\left(u\widetilde{u} + v\widetilde{v}\right)$. The angle α between the local unit vectors is given by $\sin\alpha = \|\mathbf{e_x} \times \mathbf{e_y}\|$; in an orthogonal coordinate system, $\alpha = \pi/2$.

The horizontal discretization is derived using a finite-volume integration about a 2D quadrilateral grid cell with area ΔA and over a timestep of length Δt, with the winds staggered on a D-grid (Figure 2). The discretized equations are as in Putman (2007), modified for a non-orthogonal coordinate system:

$$\delta p^{n+1} = \delta p^n + F\left[\widetilde{u^*}, \Delta t, \delta p^y\right] + G\left[\widetilde{v^*}, \Delta t, \delta p^x\right] \tag{1}$$

$$\Theta^{n+1} = \frac{1}{\delta p^{n+1}}\left\{\Theta^n \delta p^n + F\left[\widetilde{u^*}, \Delta t, (\Theta\delta p)^y\right] + G\left[\widetilde{v^*}, \Delta t, (\Theta\delta p)^x\right]\right\} \tag{2}$$

$$u^{n+1} = u^n + \Delta t\left[Y(\Omega^x) - \delta_x\left(\kappa^* - \nu\nabla^2 D\right) + \widehat{P_x}\right] \tag{3}$$

$$v^{n+1} = v^n + \Delta t\left[X(\Omega^y) - \delta_y\left(\kappa^* - \nu\nabla^2 D\right) + \widehat{P_y}\right]. \tag{4}$$

In these equations and for the remainder of the article δp, Θ, and other scalar variables are understood as cell-averaged values, and winds and fluxes as face-averaged values. The superscript n and $n+1$ represent the time-levels of the prognostic variables. The flux operators F, G, X, and Y use the contravariant C-grid winds $\widetilde{u^*}$ and $\widetilde{v^*}$, defined at the $n+\frac{1}{2}$ timelevel. The difference operator is defined as $\delta_x \eta = \eta\left(x+\frac{\Delta x}{2}\right) - \eta\left(x - \frac{\Delta x}{2}\right)$, and similarly for δ_y. The discrete Laplacian is $\nabla^2 = \delta_x^2 + \delta_y^2$.

The fluxes through a cell face are denoted $X(\widetilde{u^*}, \Delta t, \eta)$ and $Y(\widetilde{v^*}, \Delta t, \eta)$ for an arbitrary scalar η. The fluxes are computed using the piecewise-parabolic method (PPM; Colella and Woodward 1984) using the monotonicity constraint of L04. The monotonicity constraint not only eliminates unphysical overshoots in the solution but also acts as a diffusive filter that is more physically consistent than the *ad-hoc* scale-selective Laplacian diffusion or hyperdiffusion operators common in many numerical models.

The flux divergences (referred to as "outer operators" in PL07 and LR96) in each coordinate direction are:

$$
\begin{aligned}
F\left[\widetilde{u^*}, \Delta t, \eta\right] &= -\frac{\Delta t}{\Delta A}\delta_x\left[X(\widetilde{u^*}, \Delta t, \eta)\Delta y \sin\alpha\right] \\
G\left[\widetilde{v^*}, \Delta t, \eta\right] &= -\frac{\Delta t}{\Delta A}\delta_y\left[Y(\widetilde{v^*}, \Delta t, \eta)\Delta x \sin\alpha\right]
\end{aligned}
$$

for cell face lengths Δx, Δy, so that $\Delta x \sin\alpha$ is the length of a cell face in the direction perpendicular to the flux through that face. The *advective-form* inner operators, denoted by a superscript x or y, are:

$$
\begin{aligned}
\eta^x &= \frac{1}{2}\left[\eta + \frac{\eta + F\left[\widetilde{u^*}, \Delta t, \eta\right]}{1 + F\left[\widetilde{u^*}, \Delta t, 1\right]}\right] \\
\eta^y &= \frac{1}{2}\left[\eta + \frac{\eta + G\left[\widetilde{v^*}, \Delta t, \eta\right]}{1 + G\left[\widetilde{v^*}, \Delta t, 1\right]}\right].
\end{aligned}
$$

Using the inner operators to produce a scalar field which is then used in the outer operators in (1)–(4) produces a symmetric scheme which cancels the splitting error (LR96, section 2). Using advective-form operators for the inner operator does not affect mass conservation, since the outer operators are still flux-form, but allows the scheme to preserve an initially uniform mass field in a nondivergent flow and thus is more physically consistent. The denominator of the second term in the inner operators is a divergence-correction term (PL07). For a particular variable, we use the same computation for X and Y in both the inner and outer operators, which avoids a potential instability (Lauritzen 2007) in the absence of a monotonicity constraint.

The transported kinetic energy κ^* is simply $\frac{1}{2}\left[X(\widetilde{u^*}, \Delta t, u) + Y(\widetilde{v^*}, \Delta t, v)\right]$; using this form avoids the Hollingsworth-Kåallberg instability (Hollingsworth et al. 1983, LR97 pg 2481). The finite-volume absolute vorticity and divergence are given by Ω and D, respectively. Finally, the pressure gradient forces $\widehat{P_x}$ and $\widehat{P_y}$ are computed as in Lin (1997), by integrating around a 2D plane in the vertical.

The time-stepping (LR97) uses a forward-backward procedure to advance the cell-averaged values and the D-grid winds. First, the half-timestep C-grid winds $\widetilde{u^*}$, $\widetilde{v^*}$ are computed using first-order vorticity and kinetic energy fluxes, and a pressure gradient force computed using mass and potential temperature advanced to the half-timestep, also using first-order upwind fluxes. The half-timestep mass and potential temperature are then discarded. A similar procedure is performed to advance the D-grid winds, mass, and potential temperature a full timestep, using the full PPM fluxes computed from the half-timestep C-grid winds, and again using a pressure gradient force computed with pressure and temperature advanced to the $n+1$ timelevel.

Nearly any vertically-monotonic quantity can be used as the base for the Eulerian coordinate; here, we use a 32-level hybrid $\sigma - p$ terrain-following vertical coordinate, in which for given constants a_k, b_k for each layer interface $k = 1, \ldots, N+1$ and N layers, the pressure at each Eulerian layer interface is $p_k = a_k + b_k p_s$ for surface pressure $p_s = p_{N+1} = p_T + \sum_{k=1}^{N+1} p_k$ and pressure at the model top $p_T = 2.16404$ Pa ; the new δp_k in the kth layer is $p_{k+1} - p_k$. The resulting surface pressure is the same, and so this procedure conserves air mass. The remapping of other variables is done using piecewise-parabolic subgrid reconstructions in the Lagrangian layers, and then analytically integrating these over each Eulerian layer; full details are in L04. The full dynamical core does not exactly conserve total energy, but an energy "fixer" can be applied if necessary, turning all of the lost energy (including the lost kinetic energy) into heat. The remappings then not only act as vertical mass and momentum transport but also apply frictional heating to the atmosphere. Remapping need not be applied at every dynamical timestep, and indeed can be applied once every hour or even less frequently.

b. *Grid nesting methodology*

The nested grid is simply a refinement of one of the faces of the gnomonic cubed-sphere: for a refinement ratio r each coarse-grid cell is split into r^2 cells by dividing the great-circle arcs bounding each cell into r equal segments. Our nested grids are aligned with the coarse grid, making grid-coupling substantially more accurate and less complicated, but does force the nested grid to remain on one panel of the cube.

Many methods exist for nested-to-coarse grid coupling (cf. Zhang et al. 1986; Warner et al. 1997; Harris and Durran 2010). However, we will show later that our nested-grid model produces satisfactory solutions while using only simple nested grid BCs and two-way updating methods. Our boundary conditions are simply linear interpolation of the coarse-grid data, for all prognostic variables (including the half-timelevel C-grid winds) into the halo (ghost) cells of the nested grid. The BCs are updated every nested-grid timestep by linearly interpolating the coarse-grid solution between two different times.

Mass conserving two-way update methods do exist (cf. Zhang et al. 1986; Kurihara et al. 1979), but these require computation of integrals for the update and the use of often-delicate interpolated fluxes at the nested-grid boundary to correctly conserve mass. We use a much simpler approach: since δp is the mass of each layer, we simply do not include it during the two-way update. The coarse-grid pressure is undisturbed during the update and mass is trivially conserved. However, since δp also determines the vertical coordinate (even after vertical remapping, since the surface pressure gives the lowest coordinate surface) a consistent update requires us to remap the other variables—u, v, and Θ—from the nested grid's to the coarse grid's coordinates, using an appropriate extrapolation if the nested grid's surface pressure is less than the coarse grid's surface pressure. Since two-way updating already overspecifies the coarse-grid solution, and since pressure is tightly coupled to the other variables, we do not expect that not updating δp will substantially degrade the coarse-grid's solution. All simulations described in this paper will use this "mass-conserving remapping update", and are all observed to conserve mass on the coarse grid to machine precision. Since the FV core does not exactly conserve momentum, total energy, or enstrophy, we make no attempt to do so in our nesting methodology. Conservation of microphysical species or tracer mass is outside the scope of this study.

Two-way updating is done using temperature $T = \Theta p^{R/c_p}$, where R is the gas constant and c_p the specific heat at constant pressure, instead of Θ. Updating T was found to yield fewer grid artifacts, likely because unlike Θ it is not a direct function of pressure. The update is a simple areal average: the updated coarse-grid cell-averaged temperature is the average of that of the r^2 corresponding nested-grid cells it is split into. For the winds, we perform a piecewise-constant finite-volume average of the r nested-grid-cell faces along the coarse-grid face whose D-grid wind is being updated. Since the grids are aligned and each nested-grid-cell constructed out of a particular coarse-grid cell has the same dimensions, no weighting is needed when performing the average. This averaging update is more consistent with our finite-volume discretization than would a simple pointwise average, and the use of piecewise-constant finite-volume averages for the winds means that the update conserves vorticity.

While the nested model can use any integer value for the refinement ratio r, we will use a factor of 3 throughout this paper, as is traditional in atmospheric science.

3. Test cases

a. Shallow-water tests

While only a few idealized test cases exist for three-dimensional global models, an entire suite of test cases exists for two-dimensional non-linear shallow water models (Williamson et al. 1992). While we do not intend to present a full set of test cases for the shallow water version of the FV core we will present two cases which measure the nested model's ability to preserve the desirable large-scale characteristics of the single-grid's solution.

The FV core becomes a shallow water model when run with a single layer, a uniform potential temperature, and with the assumption that there is no stress from an overlying layer. Vertical remapping is unnecessary, and when performing mass-conserving two-way updating u and v are updated directly to the coarse grid.

1) Balanced geostrophic flow

Test case 2 of Williamson et al. (1992) is a flow initially in geostrophic balance, and so any deviations from the initial condition are considered errors. This test is sensitive to spatial changes in grid structure and in particular to the abrupt refinement at the nested-grid's boundary. We present tests of the model using a c48 grid—each face of the cubed-sphere is 48 grid-cells wide and has a mean grid spacing of about 210 km, or 2 degrees—which are run first for five days to create an internally-balanced initial condition (Figure 3). Errors are then characterized as the difference between the solution after another five days of integration time and this "spun-up" initial condition. The simulation uses an internal "large" timestep of 30 min, identical on both grids, corresponding to the interval between vertical remappings in a three-dimensonal model and to the interval between times used for the nested-grid BCs and for performing two-way updates. The coarse grid uses four "small" timesteps per large timestep, each corresponding to Δt for one advance of the dynamics, so the timestep for the dynamics is 7.5 min. The nested grid (depicted by a quadrilateral in Figure 3 and subsequent figures) is centered in one of the equatorial panels of the cubed-sphere, and is a refinement of the coarse grid by a factor of three ($r = 3$). The nested grid uses 12 small timesteps per large timestep. Two balanced flows, whose initial height fields (equal to $\delta p/g$) are depicted in Figure 3, are used: one with a purely zonal flow and a more stringent test with a flow field rotated 45° from zonal to allow the strongest part of the flow to pass over the corners of the cubed sphere and of the nested grid.

Although the error norms are typically twice as large in the nested-grid simulations as in the single-grid simulations (Table 1), they are still very low, representing errors of less than one part in one thousand. The absolute errors are smaller than many single-grid models of similar resolution to our coarse grid; for example, the "G5" test of the icosahedral finite-volume shallow-water model of Lee and MacDonald (2009), of comparable resolution to our c48 simulations, yields ℓ_1 and ℓ_2 errors no smaller than 10^{-4}. The errors in our nested-grid simulations were also comparable to those of the single-grid Yin-Yang multi-moment model of Li et al. (2008).

2) Rossby-Haurwitz wave

The Rossby-Haurwitz wave, Williamson test case 6, is an exact solution to the linearized shallow-water equations. This case is most interesting because the wavenumber-4 Rossby-Haurwitz wave is unstable (Thuburn and Li 2000), and truncation and roundoff errors will eventually grow and cause the wave to break. While the FV core maintains the wave well beyond 60 d even at coarse resolutions—LR97 demonstrated stability through 60 d even for a 2.5 deg resolution simulation, which we have also found for a c48 cubed-sphere simulation—many other *uniform-resolution* global models do not claim stability beyond 14 d (cf. Lee and MacDonald 2009; Li et al. 2008; Bernard et al. 2009; Lauritzen et al. 2006). While we do not expect our nested-grid model to preserve the wave for longer than a few weeks because of the unavoidable error introduced by the nested grid, we expect to retain stability at a low c48 resolution for at least 14 d, and longer at higher resolutions.

The c48 test case uses the same parameters as in the previous section. The two-way nested solution then maintains the wave for 14 d (Figure 5a) and later breaks down. If instead we use a c180 grid, in which the large timestep is reduced to 5 min on both grids and the nested grid made 180 grid cells wide in both directions (so as to cover nearly the same area as in the c48 simulations), the wave is better maintained at 14 d (Figure 5b), and does not break until after 21 d (not shown).

b. Jablonowski-Williamson baroclinic instability test

The baroclinic instability test case of Jablonowski and Williamson (2006) is a common test for three-dimensional global models to show that a reasonable baroclinic wave can be simulated in a perturbed baroclinically-unstable flow. In our nested-grid simulations we wish to show that two-way nesting does not appreciably distort the solution compared to a single-grid solution, and may even improve the representation of the baroclinic wave on the coarse grid.

The initial condition is as in Jablonowski and Williamson (2006). The cubed-sphere is rotated so that the initial perturbation, at 20 degrees east longitude and 40 degrees north latitude, is centered in one of the panels. The nested grid (seen in Figure 6) is then placed so that it covers the deepest low in the resulting baroclinic wave train at $t = 10$ d.

Our c90 simulations use a large timestep of 20 min on both grids, with 10 and 21 small timesteps per large timestep on the coarse and nested grids, respectively. The nested grid is a 3:1 spatial refinement of the coarse grid and is 96 grid cells wide in both directions. The model uses 32 levels in the vertical, using the same setup as in L04.

Results of the c90 simulations are seen in Figure 6. The nested grid is not causing any noticable distortion of the baroclinic wave compared to the single-grid c90 solution; further, additional structure has been generated by the nested grid in the deepest low's center, particularly in the 850 hPa vorticity field. A single-grid c270 simulation—one with the same resolution globally as does the nested grid in the c90 simulation—shows that the additional structure in the c90 nested simulation is real and not due to grid artifacts, although the c270 simulation has had more time at the higher resolution to develop and so is more tightly-wound than the nested-grid simulation. Examination of the nested-grid solution (Figure 7a,b) does show some low-amplitude distortion of the solution near the nested-grid boundary compared to the c270 simulation (Figure 7c,d), particularly in the vorticity field, but this does not substantially affect the solution. The nested-grid boundaries do not disrupt the strong gradients along the low's cold front, which is important because one of the major advantages of the FV core (cf. LR97, section 4) is the preservation of sharp gradients, and an effective nested-grid methodology should maintain this property. Using one-way nesting (not shown) does not make a substantial difference to the nested-grid solution, and would of course have no effect on the coarse-grid solution.

A series of c180 simulations were performed (Figure 8) using the same model parameters as the c90 simulations except that the large timestep was 10 min on both grids and used a nested grid 180 cells across to cover approximately the same area as in the c90 nested simulation. Again, the nested-grid solution is no worse than the single-grid solution, and again the nested grid is passing additional structure to the coarse grid which compares well with a c540 control simulation.

The error introduced by grid nesting can be quantified by comparing solutions to a high-resolution solution taken as "truth". As in Jablonowski and Williamson (2006) we will compute error norms in the surface pressure field on the global grid as a function of time. Here, we use a c540 single-grid simulation as our reference solution, and for comparison have also used a pair of c48 simulations. Both the single-grid and nested-grid solutions show increasing error growth during the first two weeks of the simulation (Figure 9) before the error "saturates" as both the reference and the lower-resolution simulations equilibrate and mix out their potential vorticity gradients. Both single- and nested-grid simulations show convergence at increasingly high resolutions, with no pathological error growth due to the nested grid. However, the error in the c48 nested-grid simulation is noticably larger than that of the c48 single-grid simulation during the first week, which is attributed to a spurious, smaller baroclinic wave train excited by the nested-grid boundary. This disturbance becomes increasingly small at higher resolutions, and is much smaller than the primary wave train at later times in the c48 simulation.

c. Held-Suarez climate integration

A common test for global dynamical cores is a multi-year climate integration using the Held-Suarez forcing (Held and Suarez 1994) to simulate the effects of idealized, zonally-symmetric diabatic heating and surface drag in a dry dynamical core. Here, we will test whether a nested grid disrupts the climate statistics of a single-grid model. We first present results from a pair of c48 simulations, which use the same grid (and indeed the same dynamical core) as in the GFDL AM3 (Donner and coauthors 2011) model, and has an average grid-cell width of about 200 km. The large timestep is 20 min on both grids, with 4 and 12 small timesteps per large timestep on the coarse and nested grids, respectively. The remainder of the model configuration is as for the c48 Jablonowski-Williamson test cases, except that the model grid is not rotated, and that the nested grid is again centered in one of the equatorial panels.

A useful diagnostic in the Held-Suarez simulations is the vertical velocity $\omega = \frac{dp}{dt}$, which allows us to view the strength of the meridional overturning circulations. The vertical velocity is not a prognostic variable in the FV core, but can be computed from other fields. Since at the bottom of the kth layer the pressure is $p_k = \sum_{j=1}^{k} \delta p_k + p_T$, where a subscript indicates the vertical layer index counting from the top, the total derivative of p becomes

(with use of the mass continuity equation)

$$\omega_k = \frac{dp_k}{dt} = \sum_{j=1}^{k} \frac{d}{dt}\delta p_k = \sum_{j=1}^{k} \left(\frac{\partial}{\partial t}\delta p_k + \mathbf{V}_k \cdot \nabla \delta p_k \right) \tag{5}$$

$$= \sum_{j=1}^{k} \left(-\nabla \cdot (\mathbf{V}_k \delta p_k) + \mathbf{V}_k \cdot \nabla \delta p_k \right) = \sum_{j=1}^{k} -\delta p_k \nabla \cdot \mathbf{V}_k, \tag{6}$$

or that the vertical velocity of each Lagrangian surface is the mass-weighted sum of the divergence of all overlying layers[2].

Zonal means over the last 2000 d from c48 simulations, after a 200 d model spin-up period, are shown in Figure 10. The zonal means are remarkably similar between the two simulations, and the differences between the simulations (bottom row) are small; the same is true for various eddy covariances (Figure 11). Note that the greatest difference between the nested and single grid simulations is not in the tropics, where the nested grid is located, but in the mid-latitudes. Furthermore, there is little difference between our results and those of L04, which used the latitude-longitude FV core: the most apparent difference between our c48 simulations and L04's 2° simulations (of similar resolution) is that our sub-tropical descent (Figure 10a,b) is stronger, and our sub-polar ascent weaker. Mid-latitude eddy covariances are also slightly stronger in our simulations (Figure 11), likely due to reduced implicit numerical diffusion in the cubed-sphere core.

Differences between the nested- and single-grid simulations become more apparent when examining deviations from the zonal means; since ideally the time-averaged fields should be zonally-symmetric, deviations from the zonal means are characterized as errors. These errors are most pronounced in the near-surface ω field, particularly at the cubed-sphere edges (Figure 12a,b), but are at worst an order of magnitude smaller than typical zonal-mean values of ω in the troposphere (Figure 10a,b). Errors are also apparent at the nested-grid boundary but these are again acceptably small and in fact smaller than the noise at the cube edges. At 500 hPa (Figure 12c,d) the errors at the cube edges are less extensive, and no errors due to the nested grid are apparent. Other fields show little distortion due to the nested grid:

[2]This is the discrete analogue to the formula for ω in section 3.5.1 of Holton (2004).

for example, the 500 hPa u (Figure 12e,f) shows little deviation from zonal symmetry due to grid structure. In both the nested and single-grid simulations the asymmetry between the northern and southern hemispheres, as well as deviations from zonal symmetry, decreases for longer simulations, although the grid errors are still present.

Similar results are found from a pair of c90 simulations, which are set up the same as the c48 simulations except that the large timestep is now 10 min on both grids. The zonal means (Figure 13) are very similar to the c48 simulations (Figure 10). The difference between the nested and single-grid c90 simulations is smaller than in the c48 simulations. The noise in the ω field (Figure 14a–d) due to the cubed-sphere edges and nested grid are smaller than in the c48 simulations, and again grid errors are imperceptible in other fields (Figure 14e,f).

d. Lee vortices

The final test simulates vortex shedding in the lee of the Island of Hawaii (Smith and Grubišić 1993) to determine whether the nested grid can introduce disturbances downstream of the nest caused by features that would not be resolved by the coarse grid alone. We do not aim to precisely reproduce observed vortices on a particular date, but to instead show that vortices which could not appear in a single-grid simulation can be supported on the coarse grid in a two-way nested simulation. These simulations are initialized using a T574 analysis from the National Centers for Environmental Prediction at 0000 UTC on 1 August 2010 and use 1-minute USGS topography. To prevent surface winds from being unrealistically strong, the surface drag from the Held-Suarez test described above has been applied; otherwise the model is inviscid and adiabatic. Two global grids are used: a c360 simulation with a 5 min large timestep and 10 small timesteps per large timestep, and a c120 simulation with a 10 min large timestep and 10 small timesteps per large timestep. A c120 nested-grid simulation was also performed using a 3:1 spatial refinement, so that the nested grid has the same resolution as the c360 simulation does globally, and 30 small timesteps; again, the large timestep is identical on the coarse and nested grids. The remainder of the model is formulated as in the

Held-Suarez test case.

By $t = 72$ hr there is a clear train of lee vortices apparent in the surface vorticity field in the c360 simulation (Figure 15), extending west-southwest downstream from the Island of Hawaii. Shedding occurs throughout the 96 hr-long simulation. We expect that the c120 nested simulation should have vortices form on its nested grid, but we also find that the nested grid's vortices are able to propagate out of the coarse grid and remain coherent downstream, and are slowly diffused by the dissipation in the numerics. Again, vortex shedding continues throughout the simulation. By contrast, the vortices in the single-grid c120 simulation are much weaker and poorly defined, indicating that at c120 resolution (roughly 75 km) the 150-km wide Island of Hawaii is not well-enough resolved for the processes producing lee vortices to act. The poorly-resolved topography in the single-grid c120 simulation creates much less of the baroclinically-produced vorticity needed on the flanks of the Island for vortex generation: the absolute value is at most 1.9×10^{-5} s^{-1} at $t = 72$ hr, compared to 55.1×10^{-5} s^{-1} in the single-grid c360 simulation and 25.8×10^{-5} s^{-1} on the coarse grid of the nested-grid c120 simulation. (On the nested grid, the maximum vorticity is 74.4×10^{-5} s^{-1}. This value is larger than in the single-grid c360 case because the terrain smoothing is not as strong on the nested grid, and so the mountain is somewhat steeper.) The vorticity that does appear in the single-grid c120 simulation are transients caused by the impulsive startup of the simulation, and continuous shedding does not occur.

4. Summary

Regional models have many disadvantages for climate simulation and for weather prediction on timescales of more than a few days, because unlike global models they require the specification of boundary conditions taken from a model which almost certainly has different dynamics and numerics. However, the limits of computational resources make globally-uniform high-resolution modeling impractical for most purposes. Here, we present a two-way global-to-regional nested version of the FV core allowing for better resolution over a limited area using the same model equations and discretization throughout. Our nested-grid boundary conditions and nested-to-coarse two-way update are quite simple: the boundary conditions are simple linear interpolation from the coarse-grid, and two-way updating is simply a vorticity-conserving average to corresponding coarse-grid cells of all variables except mass, allowing us to easily achieve mass conservation on the coarse grid.

Despite the simplicity of our nesting methodology, nested-grid simulations of idealized shallow-water and three-dimensional nested-grid flows demonstrate little degradation of the large-scale flow and better-simulated small-scale features compared to uniform-resolution simulations. In particular, despite an abrupt factor-of-three refinement at the nested-grid boundary the errors in a 2000-d Held-Suarez climate integration are no worse at the nest's boundary than they are at the edges of the cubed-sphere global grid. Other simulations show little distortion of the coarse-grid solution due to the presence of the nested grid; indeed, there is evidence that features resolved by the nested grid can appear on the coarse grid. This suggests that nested-grid models may be effective for including the effects of small-scale features on the larger-scale circulation, a result which was found in the nested-grid simulation of Lorenz and Jacob (2005). Examination of the nested-grid solutions reveals that there are few boundary-condition problems involving noise or reflections generated by disturbances attempting to exit the nest.

Nesting so far has been implemented and tested in idealized, dry simulations; work is planned to extend the nesting to simulations with full physics and to enable moving grids which can track a propagating disturbance, such as a tropical storm or pollutant plume. The nesting described in this paper is planned to be implemented in GFDL HiRAM (Zhao et al. 2009; Chen and Lin 2011).

Acknowledgments.

LMH was partially supported by NOAA's Hurricane Forecast Improvement Project.

Comments from Bruce Wyman and Alistair Adcroft are greatly appreciated.

REFERENCES

Atlas, R., et al., 2005: Hurricane forecasting with the high-resolution NASA finite volume general circulation model. *Geophys. Res. Lett*, **32 (3)**.

Bernard, P.-E., J.-F. Remacle, R. Comblen, V. Legat, and K. Hillewaert, 2009: High-order discontinuous galerkin schemes on general 2d manifolds applied to the shallow water equations. *Journal of Computational Physics*, **228 (17)**, 6514 – 6535, doi:DOI:10.1016/j.jcp.2009.05.046, URL `http://www.sciencedirect.com/science/article/pii/S00219991090%03143`.

Bey, I., et al., 2001: Global modeling of tropospheric chemistry with assimilated meteorology-model description and evaluation. *Journal of Geophysical Research*, **106 (23)**, 073–23.

Chen, J.-H. and S.-J. Lin, 2011: The remarkable predictability of inter-annual variability of atlantic hurricanes during the past decade. *Geophysical Research Letters*, **38 (L11804)**, 6 pp.

Chen, W., Z. Jiang, L. Li, and P. Yiou, 2011: Simulation of regional climate change under the IPCC A2 scenario in southeast China. *Climate Dynamics*, **36**, 491–507, doi:10.1007/s00382-010-0910-3, URL `http://dx.doi.org/10.1007/s00382-010-0910-3`.

Colella, P. and P. R. Woodward, 1984: The piecewise parabolic method (PPM) for gas-dynamical simulations. *J. Comput. Phys.*, **54**, 174–201.

Courtier, P. and J. Geleyn, 1988: A global numerical weather prediction model with variable resolution: Application to the shallow-water equations. *Quarterly Journal of the Royal Meteorological Society*, **114 (483)**, 1321–1346.

Delworth, T., et al., 2006: GFDL's CM2 global coupled climate models. part i: Formulation and simulation characteristics. *Journal of Climate*, **19 (5)**, 643–674.

Donner, L. and coauthors, 2011: The dynamical core, physical parameterizations, and basic simulation characteristics of the atmospheric component AM3 of the GFDL Global Coupled Model CM3. *J. Clim.*, **in press**.

Dudhia, J. and J. Bresch, 2002: A global version of the PSU-NCAR mesoscale model. *Monthly weather review*, **130 (12)**, 2989–3007.

Fox-Rabinovitz, M., J. Côté, B. Dugas, M. Déqué, and J. McGregor, 2006: Variable resolution general circulation models: Stretched-grid model intercomparison project (SGMIP). *J. Geophys. Res*, **111**, D16 104.

Giorgi, F. and L. Mearns, 1999: Regional climate modeling revisited: an introduction to the special issue. *J. Geophys. Res*, **104 (D6)**, 6335–6352.

Harris, L. and D. Durran, 2010: An idealized comparison of one-way and two-way grid nesting. *Monthly Weather Review*, **138 (6)**, 2174–2187.

Held, I. M. and M. J. Suarez, 1994: A proposal for the intercomparison of the dynamical cores of atmospheric general circulation models. *Bull. Amer. Meteor. Soc.*, **75**, 1825–1830.

Hollingsworth, A., P. Kållberg, V. Renner, and D. Burridge, 1983: An internal symmetric computational instability. *Quarterly Journal of the Royal Meteorological Society*, **109 (460)**, 417–428.

Holton, J., 2004: *An Introduction to Dynamic Meteorology*. 4th ed., Elsevier Academic Press.

Inatsu, M. and M. Kimoto, 2009: A Scale Interaction Study on East Asian Cyclogenesis Using a General Circulation Model Coupled with an Interactively Nested Regional Model. *Monthly Weather Review*, **137 (9)**, 2851–2868, doi:10.1175/2009MWR2825.1, URL `http://journals.ametsoc.org/doi/abs/10.1175/2009MWR2825.1`, `http://journals.ametsoc.org/doi/pdf/10.1175/2009MWR2825.1`.

Jablonowski, C. and D. L. Williamson, 2006: A baroclinic instability test case for atmospheric model dynamical cores. *Q. J. R. Meteorol. Soc.*, **132**, 2943–2975.

Krol, M., et al., 2005: The two-way nested global chemistry-transport zoom model TM5: algorithm and applications. *Atmos. Chem. Phys*, **5**, 417–432.

Kurihara, Y., G. Tripoli, and M. Bender, 1979: Design of a movable nested-mesh primitive equation model. *Mon. Wea. Rev*, **107 (3)**, 239–249.

Lauritzen, P. H., 2007: A stability analysis of finite-volume advection schemes permitting long time steps. *Mon. Wea. Rev.*, **135**, 2658–2673.

Lauritzen, P. H., E. Kaas, and B. Machenhauer, 2006: A mass-conservative semi-implicit semi-Lagrangian limited area shallow water model on the sphere. *Mon. Wea. Rev.*, **134**, 1205–1221.

Lee, J. and A. MacDonald, 2009: A finite-volume icosahedral shallow-water model on a local coordinate. *Monthly Weather Review*, **137 (4)**, 1422–1437.

Li, X., D. Chen, X. Peng, K. Takahashi, and F. Xiao, 2008: A Multimoment Finite-Volume Shallow-Water Model on the Yin Yang Overset Spherical Grid. *Monthly Weather Review*, **136**, 3066.

Lin, S., 1997: A finite-volume integration method for computing pressure gradient force in general vertical coordinates. *Quart. J. Roy. Meteor. Soc.*, **123**, 1749–1762.

Lin, S., R. Atlas, and K. Yeh, 2004: Global weather prediction and high-end computing at NASA. *Computing in Science & Engineering*, **6 (1)**, 29–35.

Lin, S. and R. Rood, 1996: Multidimensional flux-form semi-Lagrangian transport schemes. *Mon. Wea. Rev.*, **124**, 2046–2070.

Lin, S.-J., 2004: A 'vertically Lagrangian' finite-volume dynamical core for global models. *Mon. Wea. Rev.*, **132**, 2293–2307.

Lin, S.-J. and R. Rood, 1997: An explicit flux-form semi-Lagrangian shallow-water model on the sphere. *Q.J.R.Meteorol.Soc.*, **123**, 2477–2498.

Lorenz, P. and D. Jacob, 2005: Influence of regional scale information on the global circulation: A two-way nesting climate simulation. *Geophys. Res. Lett*, **32**.

Putman, W. M., 2007: Development of the finite-volume dynamical core on the cubed-sphere. Ph.D. thesis, The Florida State University.

Putman, W. M. and S.-J. Lin, 2007: Finite-volume transport on various cubed-sphere grids. *J. Comput. Phys.*, **227 (1)**, 55–78.

Richardson, M., A. Toigo, and C. Newman, 2007: PlanetWRF: A general purpose, local to global numerical model for planetary atmospheric and climate dynamics. *J. Geophys. Res*, **112**, 1–29.

Smith, R. and V. Grubišić, 1993: Aerial observations of Hawaii's wake. *J. Atmos. Sci.*, **50**, 3728–3750.

Thuburn, J. and Y. Li, 2000: Numerical simulations of Rossby-Haurwitz waves. *Tellus*, **52A**, 181–189.

Warner, T., R. Peterson, and R. Treadon, 1997: A tutorial on lateral boundary conditions as a basic and potentially serious limitation to regional numerical weather prediction. *Bull. Amer. Meteor. Soc.*, **78 (11)**, 2599–2617.

Williamson, D., J. Drake, J. Hack, R. Jakob, and P. Swarztrauber, 1992: A standard test set for numerical approximations to the shallow water equations in spherical geometry. *J. Comput. Phys.*, **102**, 211–224.

Zhang, D.-L., H.-R. Chang, N. L. Seaman, T. Warner, and J. Fritsch, 1986: A two-way interactive nesting procedure with variable terrain resolution. *Mon. Wea. Rev.*, **114**, 1330–1339.

Zhao, M., I. M. Held, S.-J. Lin, and G. A. Vecchi, 2009: Simulations of global hurricane climatology, interannual variability, and response to global warming using a 50-km resolution GCM. *Journal of Climate*, **22 (24)**, 6653–6678, doi:10.1175/2009JCLI3049.1, URL http://journals.ametsoc.org/doi/abs/10.1175/2009JCLI3049.1, http://journals.ametsoc.org/doi/pdf/10.1175/2009JCLI3049.1.

List of Tables

	Zonal		Rotated	
	ℓ_1	ℓ_2	ℓ_1	ℓ_2
Single-grid c48	1.68×10^{-5}	2.26×10^{-5}	4.05×10^{-5}	4.75×10^{-5}
Nested-grid c48	3.11×10^{-5}	3.98×10^{-5}	8.66×10^{-5}	1.16×10^{-4}

TABLE 1. 5-day ℓ_1 and ℓ_2 error norms for the shallow-water balanced geostrophic flow test (Williamson test case 2).

List of Figures

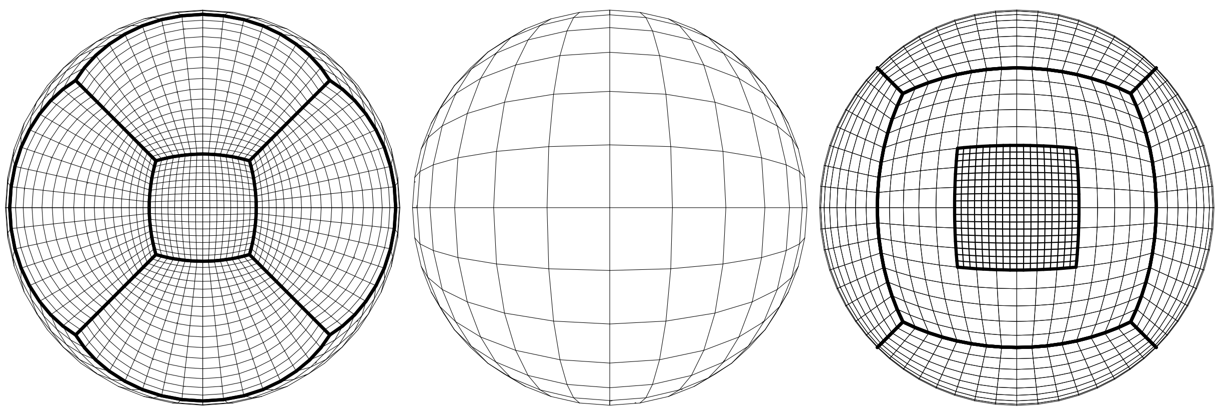

Fig. 1. Methods for locally refining a global grid. Left: A stretched cubed-sphere grid, whose smallest face has been scaled by a factor of three in both directions. Center: reverse of stretched grid showing coarsest face, which covers more than half the sphere. Right: a nested grid in an unstretched grid; the nest is a three-to-one refinement of the coarse grid. Thin lines represent local coordinate lines; heavy lines represent cube edges and nested-grid boundaries.

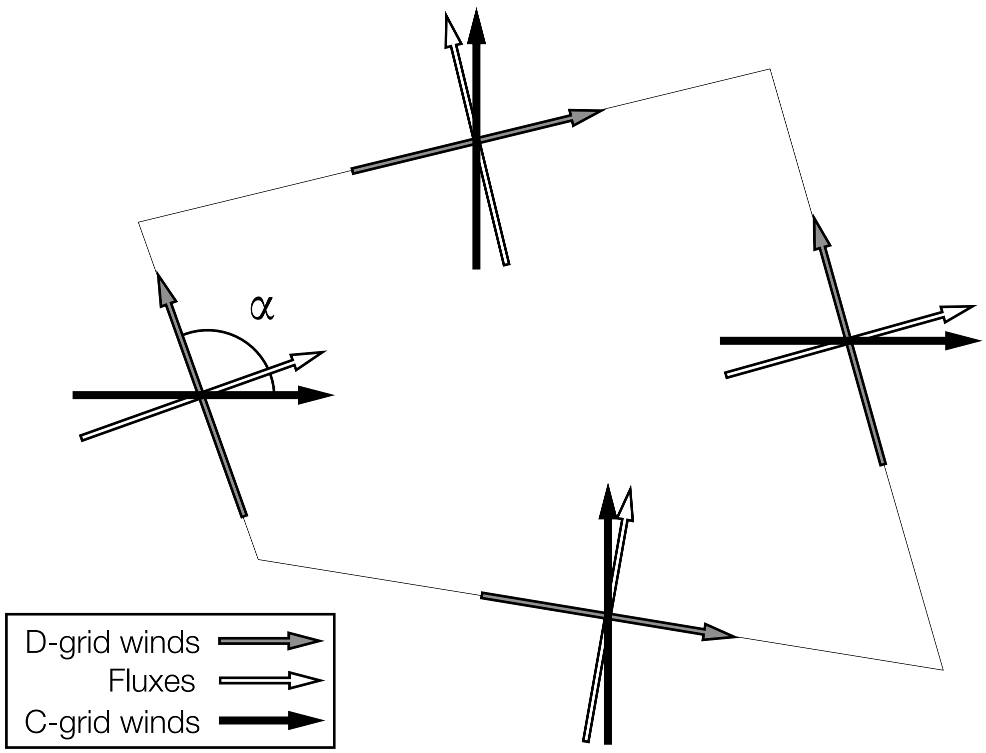

FIG. 2. Geometry of the wind staggerings and fluxes for a cell on a non-orthogonal grid. The angle α is that between the covariant and contravariant components; in orthogonal coordinates $\alpha = \pi/2$.

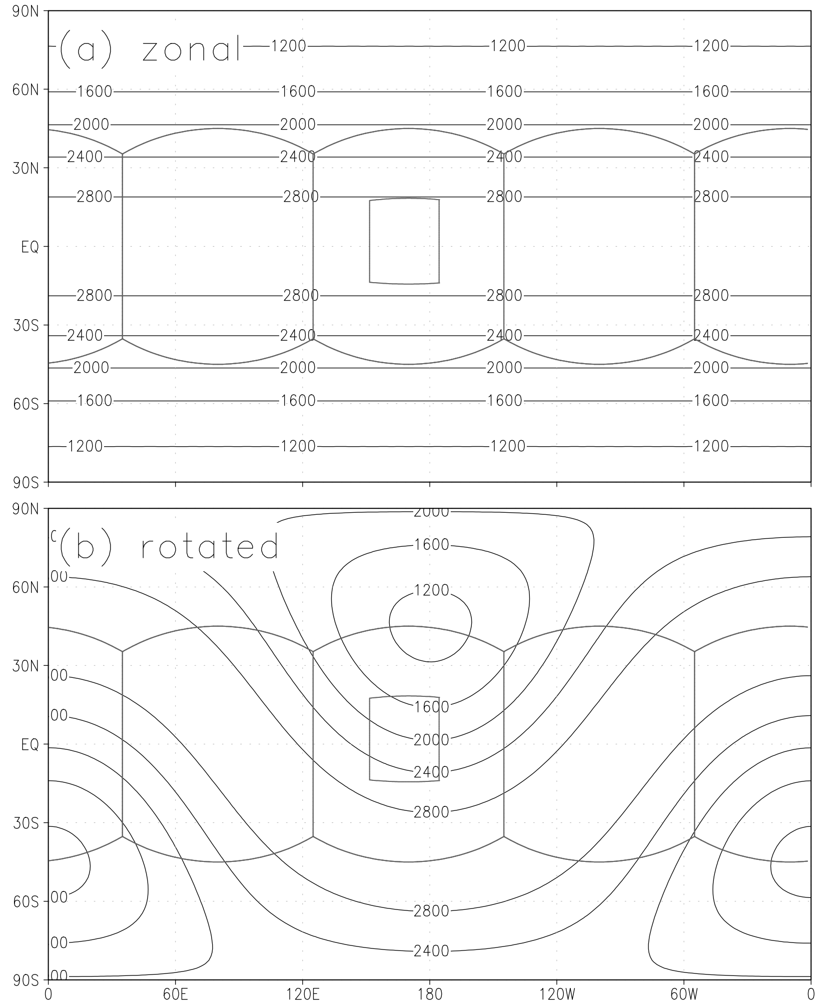

Fig. 3. Initial height field for the shallow-water balanced geostrophic flow test (Williamson test case 2). Contour interval is 400 m. 'Rotated' in (b) refers to the flow rotated 45° from zonal. In this and all other figures gray curves indicate boundaries of the cubed-sphere panels and of the nested grid, when present.

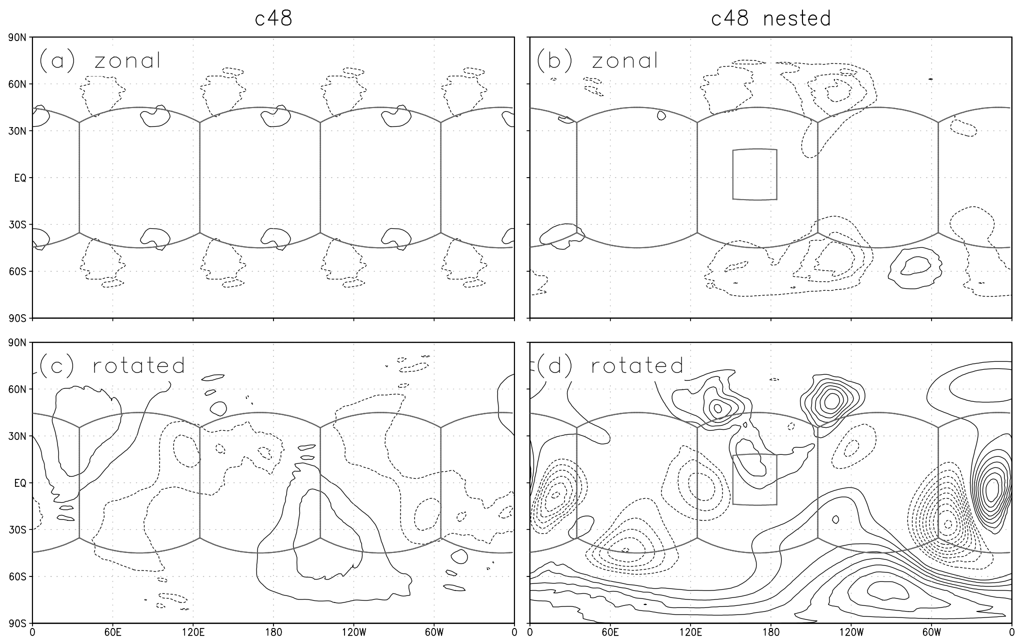

FIG. 4. *Absolute* 5-day height errors for the shallow-water balanced geostrophic flow test (Williamson test case 2). Contour interval is 0.1 m, negative values dashed, zero contour suppressed.

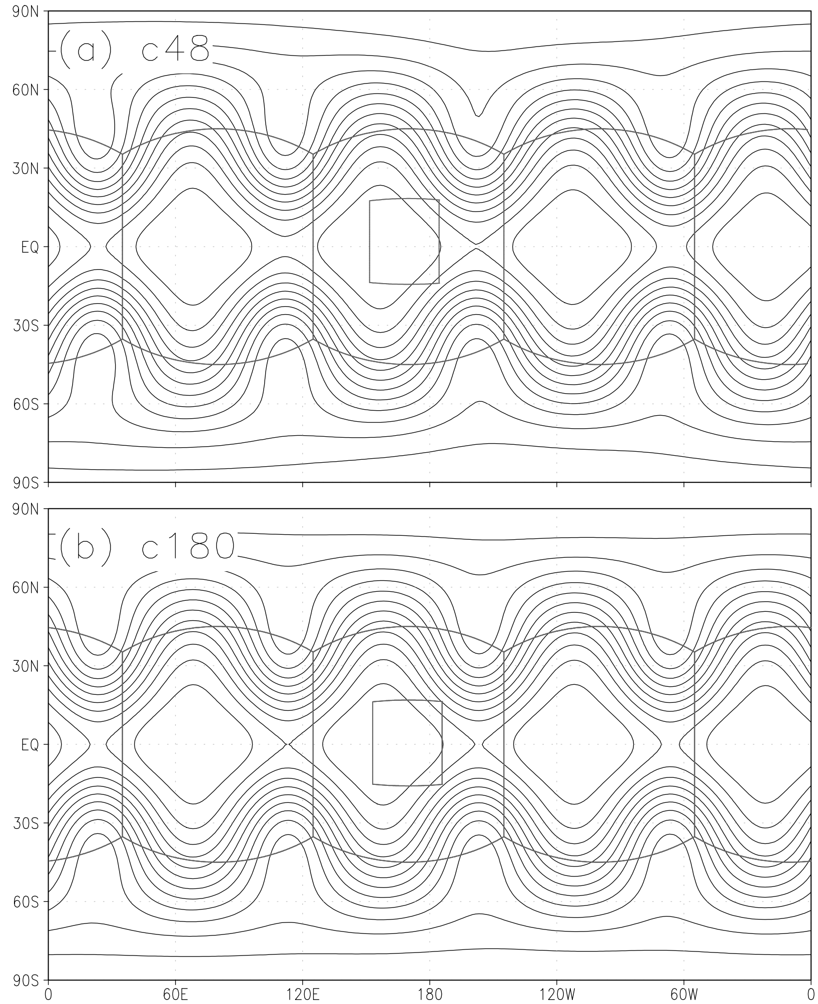

FIG. 5. Height at 14 d in the shallow-water Rossby-Haurwitz wave test (Willianson test case 6, contour interval = 2 m) for a (a) c48 nested grid simulation and (b) a c180 nested grid simulation.

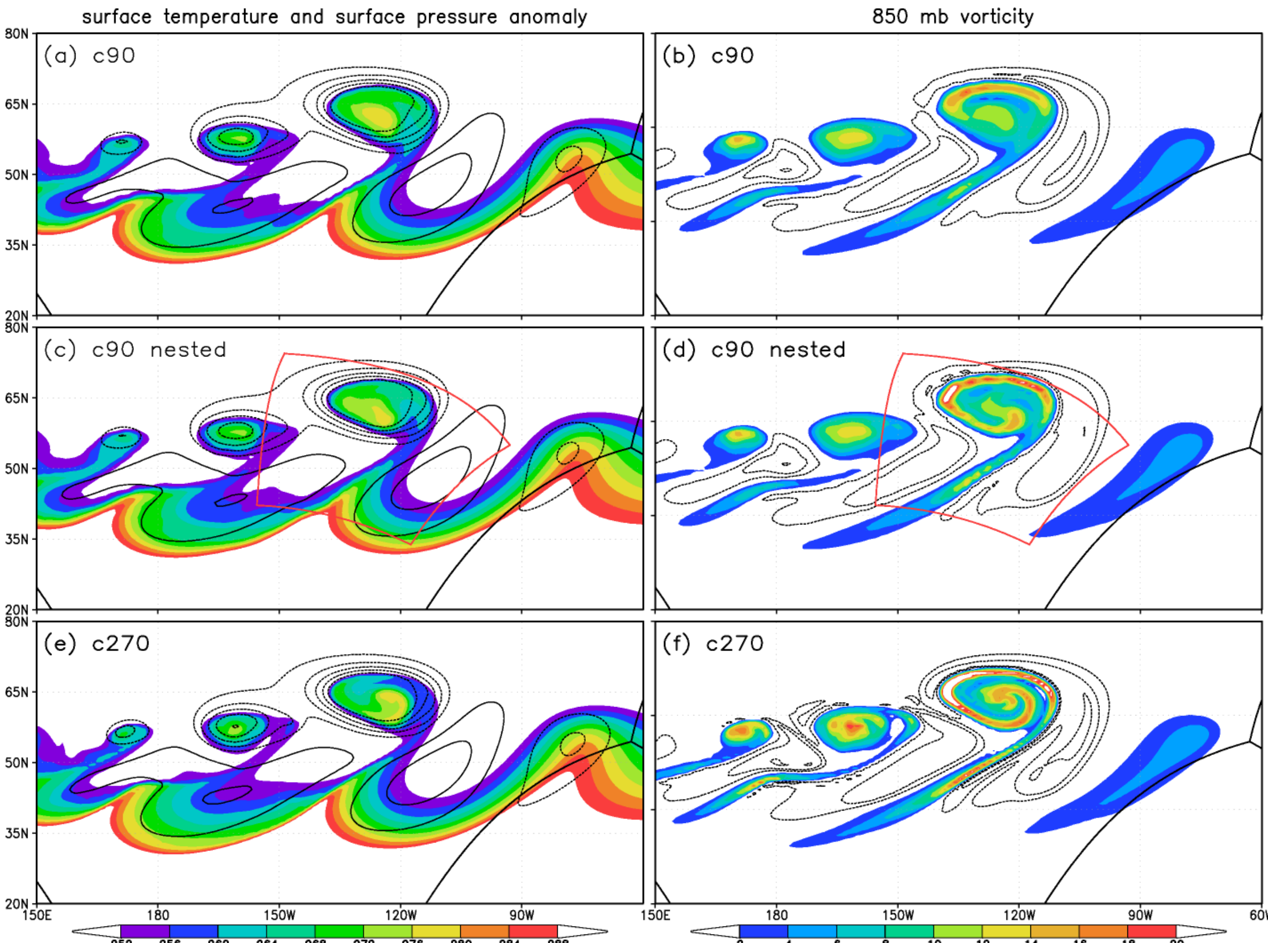

FIG. 6. Jablonowski-Williamson test case solutions at c90 resolution for a single-grid simulation (panels a, d) and a nested-grid simulation (panels b, e), and at c270 resolution (panels c, f). Panels (a–c) show surface temperature (K, color) and pressure perturbation (contour interval 4 hPa, negative values dashed); panels (d–f) show 850 hPa absolute vorticity (positive values in color, negative values contours of interval 20^{-5} s^{-1}). Here, the nested grid is outlined in red.

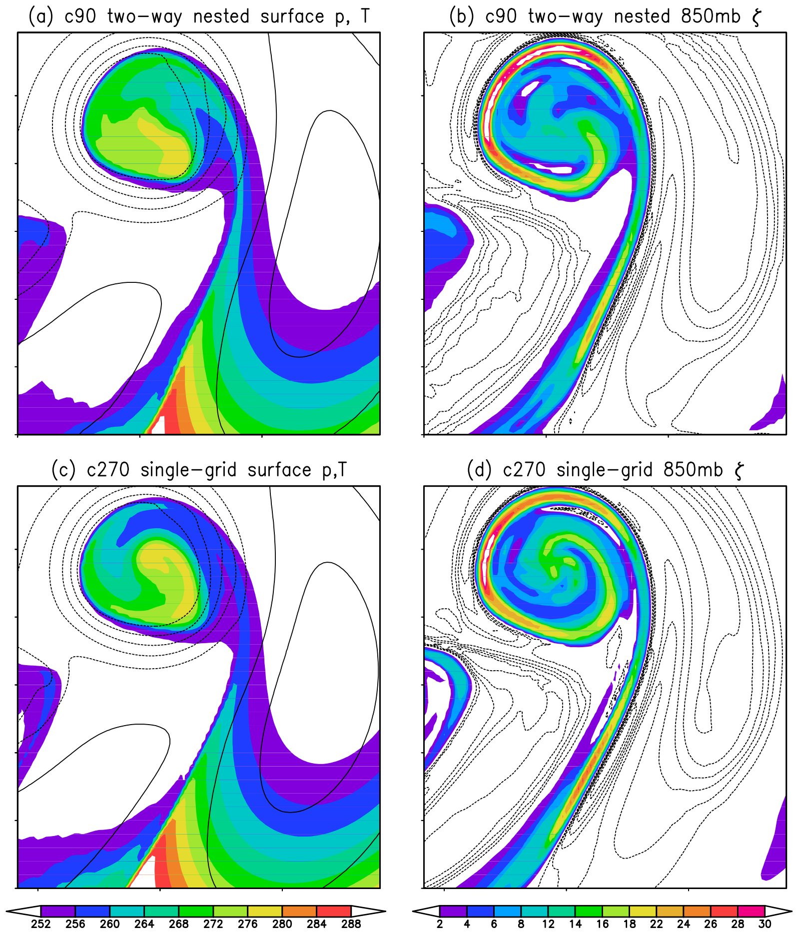

FIG. 7. Jablonowski-Williamson test case solutions on the nested grid at c90 resolution for a two-way nest (panels a, b) and over the same area for the c270 resolution single-grid simulation (panels e, f). Panels (a,c,e) show surface temperature (K, color) and pressure perturbation (contour interval 4 hPa, negative values dashed); panels (b,d,f) show 850 hPa absolute vorticity (positive values in color, negative values contours of interval 10^{-5} s^{-1}).

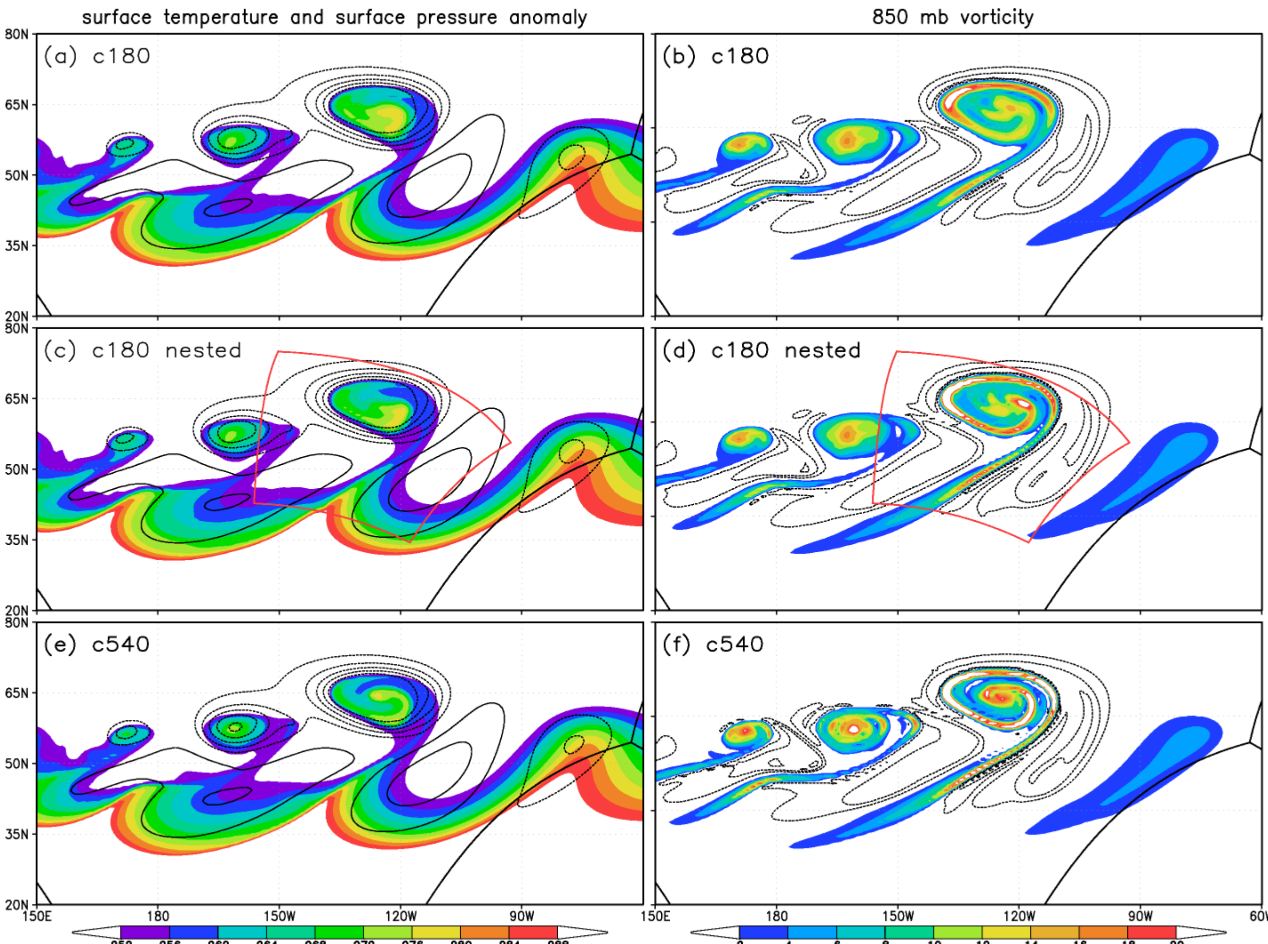

FIG. 8. As in Figure 6 but at c180 resolution (panels a–d) and c540 resolution (panels e,f).

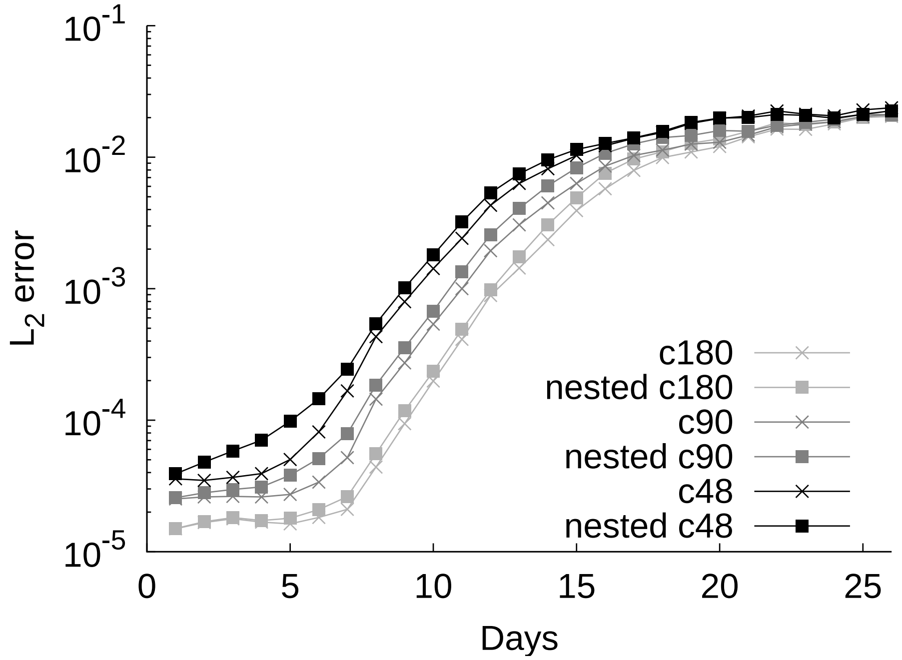

FIG. 9. Jablonowski-Williamson test case surface-pressure ℓ_2 errors relative to a c540 simulation. Single-grid simulations are indicated by crosses; nested-grid simulations are indicated by filled squares.

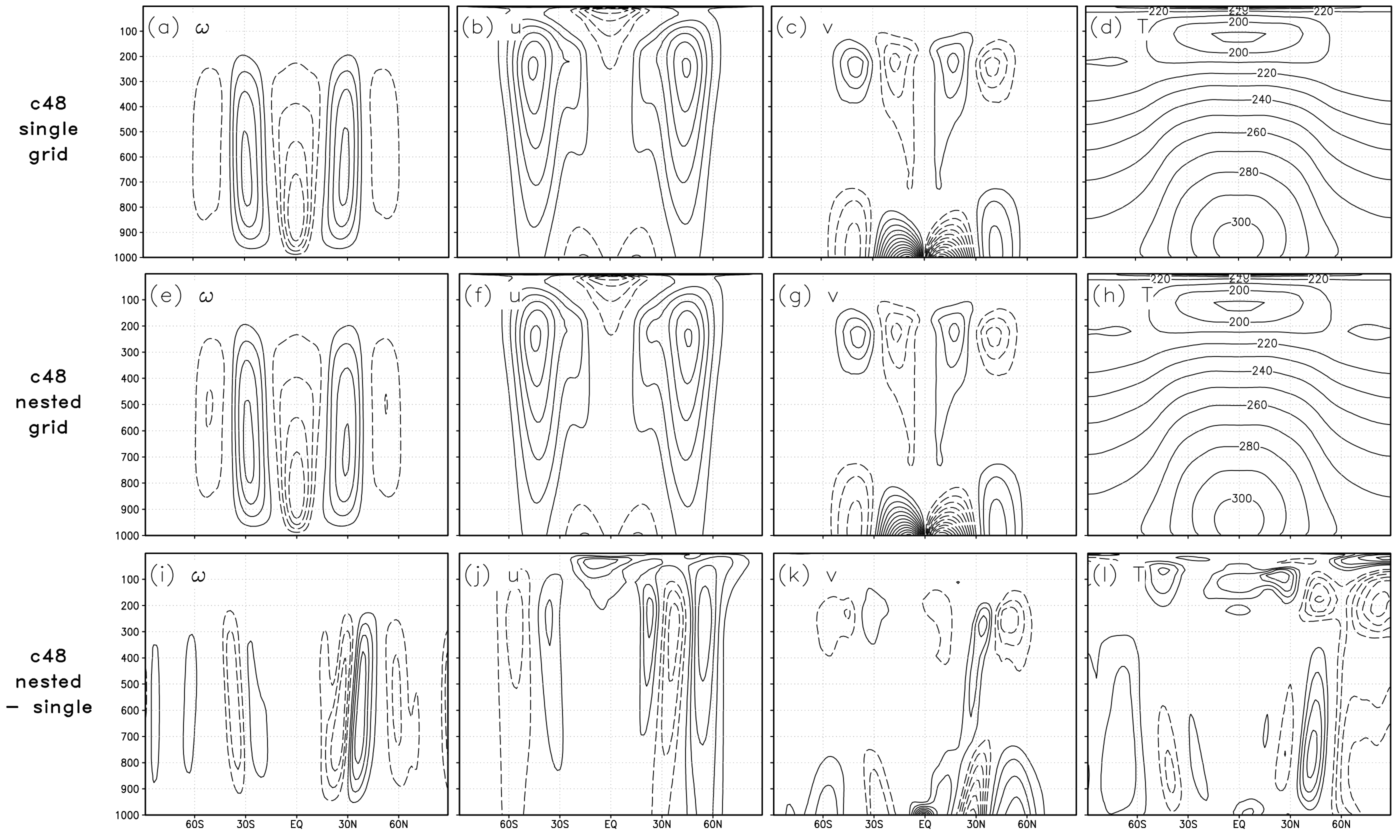

Fig. 10. 2000-d averaged c48 Held-Suarez simulation zonal means: single-grid simulation (a) ω (contour interval 5 hPa d^{-1}), (b) u (5 m s^{-1}), (c) v (0.25 m s^{-1}), (d) T (10 K). Panels (e–h) depict the same as in (a–d) except for the nested-grid simulation. Panels (i–l) depict the difference between the nested and coarse-grid simulations; contour intervals are (i) 0.5 hPa d^{-1}, (j) 0.5 m s^{-1}, (k) 0.02 m s^{-1}, and (l) 0.1 K. In all panels negative values are dashed and the zero contour has been suppressed.

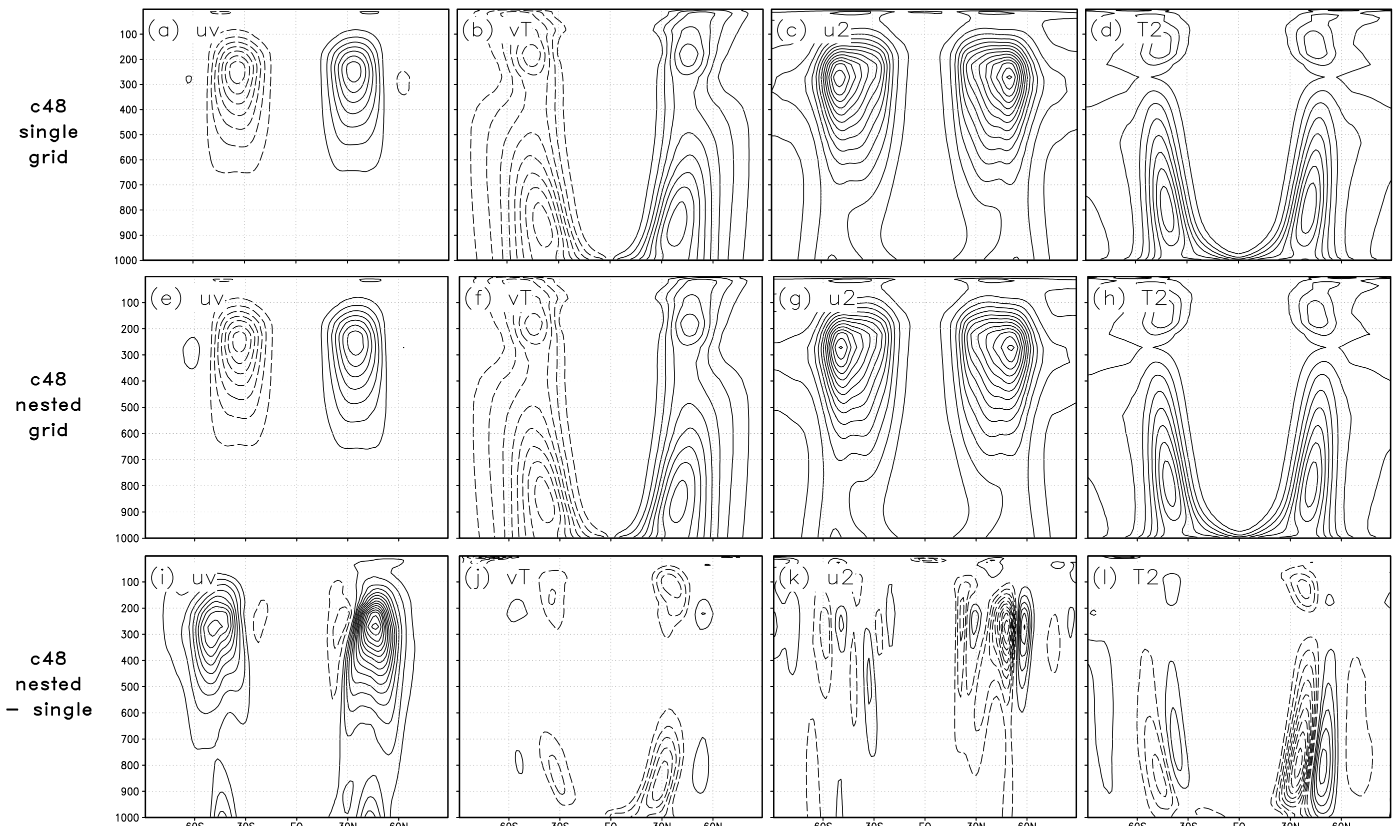

Fig. 11. 2000-d averaged c48 Held-Suarez simulation eddy statistics: single-grid simulation (a) meridional flux of zonal momentum (contour interval 10 m^2 s^{-2}); (c) meridional heat flux (2.5 K m s^{-1}); (e) zonal wind variance (20 m^2 s^{-1}, largest contour 260 m^2 s^{-1}); and (g) temperature variance (5 K^2, largest contour 40 K^2). Panels (e–h) depict the same as in (a–d) except for the nested-grid simulation. Panels (i–l) depict the difference between nested and coarse-grid simulation; contour intervals are (i) 0.5 m^2 s^{-2}, (j) 0.2 K m s^{-1}, (k) 2 m^2 s^{-1}, and (l) 0.5 K^2. In all panels negative values are dashed and the zero contour has been suppressed.

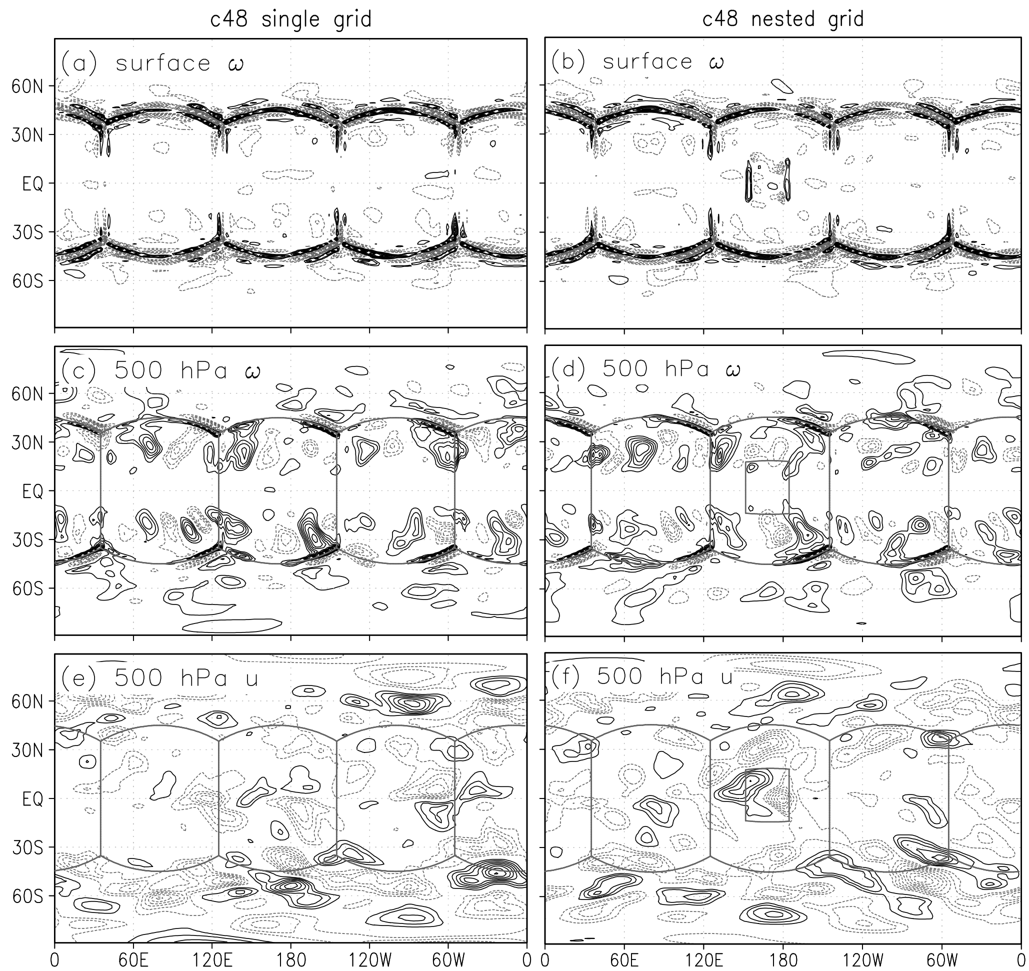

FIG. 12. 2000-d averages, with zonal means removed, for (a,b) lowest model-level ω/ω_0 (contour interval 0.01); (c,d) 500 hPa ω/ω_0 (0.1); and (e,f) 500 hPa u/u_0 (0.01), in c48 single-grid (a,c,e) and nested-grid (b,d,f) simulations. Characteristic velocities are $\omega_0 = 10$ mb d^{-1} and $u_0 = 10$ m s^{-1}. In all panels the zero contour has been suppressed for clarity, as has been the grid geometry in (a) and (b), and negative values are plotted in gray.

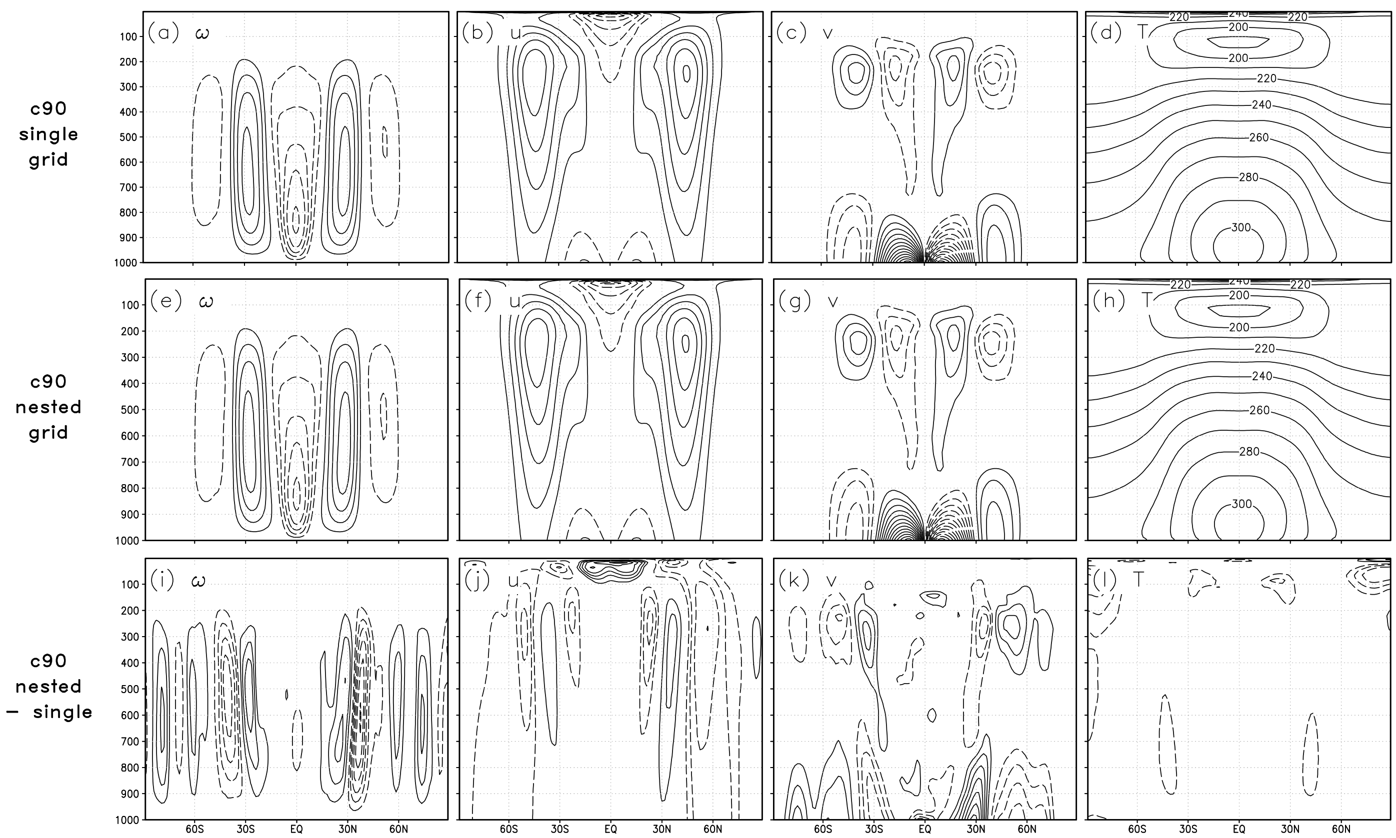

Fig. 13. As in Figure 10 but for c90 simulations.

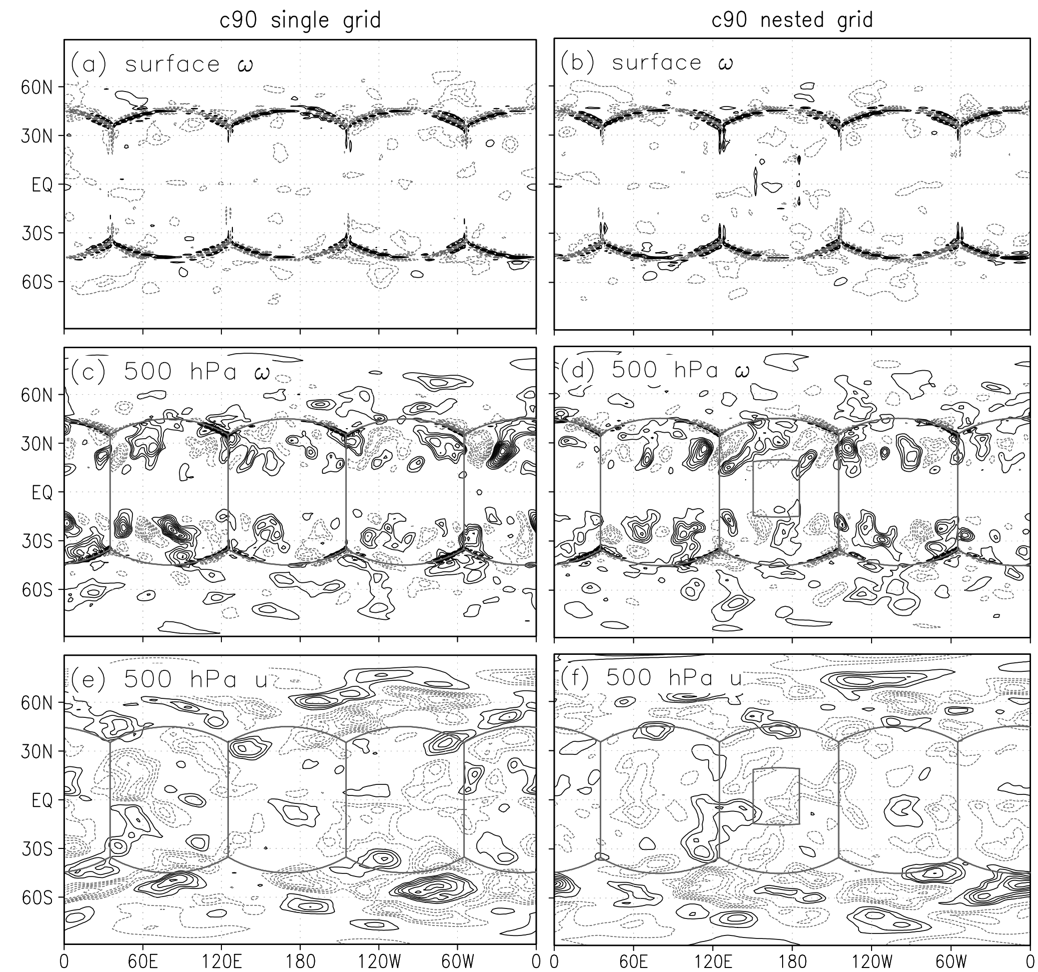

FIG. 14. As in Figure 12 but for c90 simulations.

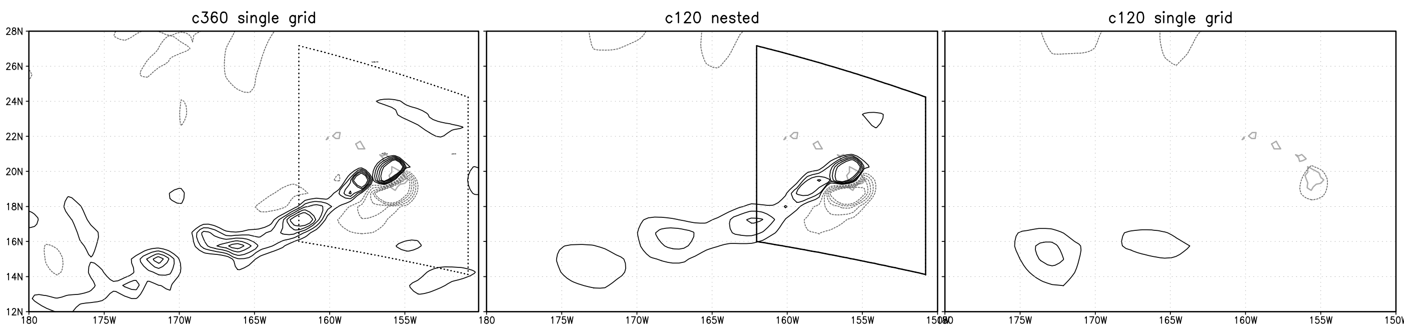

FIG. 15. Surface vorticity (contour interval 10^{-5} s^{-1}, negative values in gray, values above 5×10^{-5} s^{-1} not plotted) at $t = 72$ h in simulations initialized at 0000 UTC on 1 August 2010. Hawaii is at center-right in each panel. Dotted line in left-most panel shows where the nest would be in the nested-grid c120 simulation.